Journal of Geophysical Research: Solid Earth

Supporting Information for

Theoretical predictions vs environmental observations on serpentinization fluids: Lessons from the Samail ophiolite in Oman

J. A. M. Leong[1,2], A. E. Howells[1,3], K. J. Robinson[1,4], A. Cox[5], R. V. Debes II[1,2], K. Fecteau[1,4], P. Prapaipong[1,2], and E. L. Shock[1,2,4]

[1]Group Exploring Organic Processes In Geochemistry (GEOPIG)
[2]School of Earth & Space Exploration
[3]School of Life Sciences
[4]School of Molecular Sciences
Arizona State University
Tempe, AZ 85287, USA

[5]Laboratory Exploring Geobiochemical Engineering and Natural Dynamics (LEGEND)
Montana Technological University
Butte, MT 59701, USA

Contents of this file

Additional Supporting Information (Files uploaded separately)

Introduction

Computational models used in this work and previously described in Leong and Shock (2020) are summarized in this supplementary document (Section S1). Furthermore, additional details on statistical methods applied to analytical results are also presented (Section S2). Fluids sampled from gabbroic bodies in the Samail ophiolite, which were not discussed in the main text, are described in this supporting document (Section S3). Supplementary figures and tables that depict results of analytical (Figures S1–S3, S5, and S7–S8; Tables S1 and S2), theoretical (Figures S2, S5, and S7–S8; Table S2), and statistical methods (Figure S6; Tables S3–S5) are also presented. Compositions of end-member fluids used in mixing calculations conducted in this work are compiled in Table S6.

S1. Computational Model

S1.1. Model Setup

Reactions that drive the transformation of rainwater to fluids that are reduced and hyperalkaline occur through progressive reactions with ultramafic rocks, which can be tracked using reaction-path calculations. These calculations simulate reactions of minerals with a fluid and determine the compositions of coexisting solid phases and fluid constituents attained at thermodynamic equilibrium at various extents of overall reaction progress. Progress of the alteration process is related to an increase in the rock-to-water ratio, simulating a given mass of fluid reacting with more rock as it infiltrates deeper into the subsurface. Following Cipolli et al. (2003) and Paukert et al. (2012), the model starts as a system *open* to atmospheric exchange and then transitions into a system *closed* to input from the atmosphere, simulating fluid pathways infiltrating deeper into the aquifer. Simulations were run with a fluid-centered, flow-through physical system that tracks compositions as fluid reacts with rock. For the composition of the starting fluid, a global average rainwater composition compiled by Hao et al. (2017) from Berner and Berner (2012) was used. Reacting rocks have starting compositions typical of harzburgites common in the Oman ophiolite (Hanhoj et al., 2010) and are composed mostly of olivine (>60 mol%) with some orthopyroxene (<40 mol%) and minor amounts of clinopyroxene (<5 mol%). In the initial models, inputs from primary minerals are controlled by relative dissolution rates. Calculations were then performed where experimentally-derived dissolution rates of the primary minerals are used to assess timescales needed to reach various stages of the overall serpentinization progress.

Aside from reaction paths, concentrations of solutes at a given pH in equilibrium with various serpentinization-relevant minerals (brucite, magnesite, calcite, serpentine, etc.) were calculated. Dissolved Mg concentrations in equilibrium with brucite at a given pH was determined, and predicted Mg concentrations constrained by the solubility of magnesite were also calculated. DIC levels in equilibrium with magnesite at given pH and Mg values were determined using charge balance. Similar calculations were performed to determine the dissolved Ca and DIC concentrations of fluid in equilibrium with calcite. Dissolved Si concentrations in equilibrium with serpentine (chrysotile) were determined using calculated Mg values in equilibrium with magnesite at pH <10 and brucite at pH >10.

The solubility-reaction path program EQ3/6 (Wolery and Jarek, 2003) with a customized thermodynamic database was used for these calculations. Thermodynamic data used in the calculations were calculated with the SUPCRT code (Johnson et al., 1992) using standard state thermodynamic data for aqueous species taken from Shock and Helgeson (1988), Shock et al. (1989, 1992, 1997), and Sverjensky et al. (1997), together with the revised Helgeson-Kirkham-Flowers equations of state (Shock et al., 1992). Data for minerals were mostly taken from Helgeson et al. (1978) and Wolery and Jove-Colon (2004) with the addition of estimated standard Gibbs energies of formation of Fe end-members of several serpentinization-relevant Mg- and Fe-bearing minerals. Data for these minerals were added, while maintaining internal thermodynamic consistency, to explore solid solution behavior during serpentinization. These data, including discussion of data sources, can be found in Leong and Shock (2020), which includes a wider range

of model results that encompass the effects of variable temperatures (0–100°C), compositions of reacting ultramafic rocks, fluid salinity, and buffering capacities of serpentinization-relevant minerals.

S1.2. Model Results: Stages of the serpentinization reaction progress

Results of calculations simulating the serpentinization of an ultramafic rock of the composition 85% olivine (Forsterite$_{90}$, $Mg_{1.8}Fe_{0.2}SiO_4$), 14% orthopyroxene (Enstatite$_{90}$, $Mg_{0.9}Fe_{0.1}SiO_3$), and 1% clinopyroxene (Diopside$_{95}$, $CaMg_{0.95}Fe_{0.05}Si_2O_6$) at ambient conditions (25°C, 1 bar) are shown in Figure S4. Results of simulations with other olivine-rich compositions yield similar trends as demonstrated by Leong and Shock (2020). Consequences of variable temperatures (0–100°C) and increasing pyroxene abundance on the compositions of the coexisting fluid and solid precipitates are also described in detail in the same study. The calculated increase in pH with reaction progress is shown in Figure S4a, and changes with increasing pH in the total concentrations of Ca, Mg, Si, Fe, and dissolved inorganic carbon (DIC), as well as the number of moles of secondary minerals produced or consumed, are depicted in Figures S4b and S4c, respectively. Calculated reaction paths are depicted in activity diagrams that show the stabilities of minerals relative to the activities of aqueous solutes in the MgO-SiO_2-H_2O (Figure S4d) and CaO-MgO-SiO_2-H_2O (Figure S4e) systems.

The predicted reaction path shown in Figure S4 can be divided into six general stages as indicated by the circled numbers that depict the starting points of these various stages. These stages are discussed in detail by Leong and Shock (2020) and summarized below where the phrases in italics encapsulate each stage.

(1) The *dissolution of primary minerals into rainwater* begins when rainwater reacts with ultramafic rocks that are formed in the Earth's mantle. When transported to the surface through tectonic events, ultramafic rocks are unstable and are readily altered in the presence of aqueous fluids. Rain is slightly acidic and contains protons derived from atmospheric $CO_{2(g)}$ via

$$\mathrm{CO_{2(g)} + H_2O \Leftrightarrow HCO_3^- + H^+} \quad \text{(S1)}$$

which drive the dissolution of primary minerals present in ultramafic rocks through hydrolysis reactions. Consumption of protons during mineral hydrolysis increases pH as illustrated in Figure S4a. Dissolution of minerals yields solutes to the fluid, driving an increase in the total Mg, Si, and Ca concentrations, as depicted in Figure S4b. The fluid pathway is open to atmospheric exchange and consequently, reaction S1 dictates that the DIC must increase with pH to maintain equilibrium with a constant atmospheric $fCO_{2(g)}$ of ~$10^{-3.5}$. The increase in DIC during this stage is depicted in Figure S4b. As shown in Figure S4c, no minerals except for an oxyhydroxide (goethite) precipitate at this stage. Also shown in the activity diagrams depicted in Figures S4d and S4e, the increase in pH and total Mg, Si, and Ca will drive the reaction path toward higher $a\mathrm{Mg^{+2}}/(a\mathrm{H^+})^2$ and $a\mathrm{Ca^{+2}}/(a\mathrm{H^+})^2$ (activity ratios) as well as higher $a\mathrm{SiO_{2(aq)}}$ (silica activity). This stage marks the transition from a slightly acidic and dilute rainwater to a circumneutral (pH 7-8) fluid enriched in Mg^{+2} and HCO_3^-.

(2) The *onset of serpentinization* occurs as the solution is concentrated enough to precipitate serpentine, as represented by the mineral chrysotile. Quartz and talc can also be saturated at this stage, but the formation of these minerals was suppressed in the

model to evaluate the maximum silica activity and total Si concentration attained when serpentine saturation is achieved, which occurs when the reaction path reaches the chrysotile saturation line as shown in Figure S4d. The precipitation of chrysotile from solutes, as depicted by the reaction

$$3Mg^{+2} + 2SiO_{2(aq)} + 5H_2O \rightarrow Mg_3Si_2O_5(OH)_{4(chrysotile)} + 6H^+, \quad (S2)$$

consumes Si and causes a decrease in its concentration as depicted in Figure S4b. Precipitation of chrysotile also causes the reaction path depicted in Figure S4d to shift to lower silica activity along the chrysotile saturation line. Despite the consumption of Mg through reaction (S2), continuing dissolution of olivine-dominated rocks results in a surplus of Mg with respect to Si consumed during serpentinization as depicted by

$$2Mg_2SiO_{4(forsterite)} + 2H^+ + H_2O \rightarrow Mg_3Si_2O_5(OH)_{4(chrysotile)} + Mg^{+2}, \quad (S2)$$

leading to further increases in aqueous Mg at this stage. The pH continues to increase despite the release of protons during serpentine formation (reaction S2), as it is not enough to counter their consumption during the dissolution of primary minerals as exemplified by reaction (S3). Nevertheless, in addition to reaction (S1), the release of protons through precipitation reactions (e.g., reaction S2) can drive further dissolution and thus overall reaction progress.

(3) As fluids infiltrate deeper into the subsurface, a *transition from an open to a closed system* occurs. As shown in Figure S4a, a sharp increase in pH occurs once the atmosphere no longer supplies protons via reaction (S1). The increase in pH, as well as the increasing concentrations of Mg and Ca, will result in the *precipitation of carbonates*. As shown in Figure S4c, the first carbonate to precipitate is dolomite followed by magnesite, the latter forming more abundantly than the former. As shown in Figure S4b, the precipitation of these Mg- and Ca-bearing carbonates drives a decrease in the DIC and the total Ca and Mg concentrations.

(4) *Brucite saturation* is attained once the pH is high enough (pH ~ 10). As shown in Figure S4d, brucite precipitation occurs at extremely low $a SiO_{2(aq)}$ where the trend of decreasing $a SiO_{2(aq)}$, observed since the onset of serpentinization at Stage 2, stops at the intersection of the brucite and chrysotile saturation lines. In Figure S4e, this corresponds to where the reaction path encounters the boundary between the chrysotile and brucite stability fields. From this point onward in overall reaction progress, the $a SiO_{2(aq)}$ of the solution will be fixed by an equilibrium assemblage of chrysotile and brucite (Ctl-Brc) depicted by the reaction

$$3Mg(OH)_{2(brucite)} + 2SiO_{2(aq)} \Leftrightarrow Mg_3Si_2O_5(OH)_{4(chrysotile)} + H_2O. \quad (S4)$$

Despite the $a SiO_{2(aq)}$ being fixed by reaction (S4), the speciation of Si allows for an increase in total dissolved Si, as depicted in Figure S4b, because the abundance of $HSiO_3^-$ and consequently the total Si concentration increases with increasing pH to maintain equilibrium with the reaction

$$SiO_{2(aq)} + H_2O \Leftrightarrow HSiO_3^- + H^+. \quad (S5)$$

The precipitation of brucite causes an abrupt decrease in the total Mg concentration, as depicted in Figure S4b. Together with deceasing DIC, decrease in Mg concentration causes magnesite and, eventually, dolomite to stop precipitating as shown in Figure S4c. On the other hand, the total Ca concentration increases as more Ca is

released into the fluid from the dissolution of clinopyroxene relative to its uptake through the precipitation of dolomite. This stage marks the transition from a fluid enriched in Mg and DIC to an increasingly alkaline and Ca-rich solution.

(5) In addition to becoming more alkaline, *fluids can become more reduced* as H_2 is generated from the oxidation of ferrous iron from the primary minerals to ferric iron in secondary minerals coupled with the reduction of water to H_2 as depicted by the generalized reaction

$$2\mathrm{Fe(II)O}_{(\text{primary minerals})} + \mathrm{H_2O} \rightarrow \mathrm{Fe(III)_2O_{3(secondary\ minerals)}} + \mathrm{H_{2(aq)}}. \quad \text{(S6)}$$

At these reduced conditions, the main iron-hosting secondary mineral transitions from goethite to magnetite (Figure S4c). The results shown in Figure S4 are from a calculation without considering the incorporation of Fe into solid solutions of serpentine and brucite. If allowed, formation of magnetite is less favored, and most of the iron is incorporated into ferrous and ferric iron-bearing serpentine and ferrous iron-bearing brucite (see McCollom and Bach, 2009; Klein et al., 2009; 2013; 2014; Leong and Shock, 2020). Formation of methane is also favored at these reduced conditions. When not kinetically inhibited, the formation of methane will drive DIC to extremely low concentrations ($<10^{-12}$ molal). If abiogenic methane formation is kinetically inhibited, as it is likely to be at low-temperature conditions (Shock, 1992; McCollom, 2016; Wang et al., 2018) or in gas-poor systems (McCollom, 2016; Etiope and Whiticar, 2019), DIC can persist in solution at low but detectable concentrations (~10 μmolal) as depicted in Figure S4b. Increasing pH and Ca concentration will saturate calcite (Figure S4c). As the DIC concentration is minimal at this stage of the reaction progress, the amount of precipitating calcite will not be enough to counter the increasing Ca concentration brought about by the increasing amount of clinopyroxene dissolved. With increasing pH and total Ca concentration, the reaction path depicted in Figure S4e follows an increasing trajectory in $a\mathrm{Ca}^{+2}/(a\mathrm{H}^{+})^2$ along the boundary between the chrysotile and brucite stability fields until it reaches equilibrium with diopside.

(6) *Chrysotile-Brucite-Diopside (Ctl-Brc-Di) equilibrium* is attained when the reaction path depicted in Figure S4e reaches the point where the stability fields of chrysotile, brucite and diopside meet. So far, since the beginning of Stage 1, release of protons through precipitation reactions is not enough to counter its consumption through dissolution reactions, hence pH continues to increase. Throughout overall reaction progress, releases of Mg and Si through the dissolution of primary minerals are mostly incorporated into precipitating serpentine, brucite, magnesite, and dolomite. On the other hand, especially during the latter stages of overall reaction progress, dissolved Ca will continue to accumulate in the fluid despite its incorporation into dolomite and calcite owing to the very low amount of DIC remaining in solution. The release of Ca^{+2} into the solution from the dissolution of diopside is accommodated by the loss of H^{+} (or depending on how the precipitation and dissolution reactions are written, release of OH^{-}) and causes the continuous increase in pH. The increasing pH trend stops when the fluid reaches equilibrium with diopside, as shown by point 6 in the activity diagram depicted in Figure S4e. At this point, diopside dissolution is no longer favorable. Moreover, the equilibrium assemblage of chrysotile, brucite and diopside (Ctl-Brc-Di), depicted by the reaction

$$CaMgSi_2O_{6(diopside)} + 2Mg(OH)_{2(brucite)} + 2H^+ \Leftrightarrow Ca^{+2} + Mg_3Si_2O_5(OH)_{4(chrysotile)} + H_2O, \quad \text{(S7)}$$

corresponds to an invariant point in the CaO-MgO-SiO_2-H_2O system. Thus, not only the pH (Figure S4a) but also the Ca, Mg, and Si concentrations (Figure S4b) will remain unchanged despite continuing reaction progress, until diopside is completely reacted. As Ctl-Brc equilibrium (Stage 4, Figure S4d) ensures that the fluids stay undersaturated or out of equilibrium with forsterite (olivine) and enstatite (orthopyroxene) at low temperatures, fluids attaining equilibrium with diopside (clinopyroxene) are as close as possible to being in equilibrium with ultramafic rocks, and thus define the final stage, Stage 6, of overall serpentinization progress. Reaction S7 also constrains the maximum pH allowed in serpentinizing environments (~12.2 at 25°C and 1 bar), explaining why extremely alkaline environments (pH >13) are rare during ultramafic weathering (Leong & Shock, 2020).

Trends depicted in Figure S4 apply to reactions with olivine-rich lithologies. Greater contributions from orthopyroxene will generate fluids that first equilibrate with chrysotile and diopside before attaining brucite saturation. In the activity diagram depicted in Figure S4e, these reaction paths will track along the chrysotile-diopside boundary before reaching the Ctl-Brc-Di invariant point. Eventually, significant contributions from orthopyroxene (50–60 mole %) will yield fluids that end up at the chrysotile-tremolite-diopside (Ctl-Tr-Di) invariant point. Even greater (>60% mole %) orthopyroxene contribution will yield fluids in equilibrium with chrysotile-talc-tremolite (Ctl-Tlc-Tr). The latter two equilibrium assemblages imply higher $a SiO_{2(aq)}$ and lower $a Ca^{+2}/(a H^+)^2$ activity ratios compared to Ctl-Brc-Di equilibrium, as depicted in Figure S4e, generating more Si-rich and less alkaline fluids. Dissolution of secondary minerals such as serpentine and brucite and relict clinopyroxene in partially serpentinized ultramafic rocks can also lead to Ctl-Brc-Di equilibrium, especially if brucite is still abundant. Lower amounts of reacting brucite can lead to reaction paths ending at the Ctl-Tr-Di or the Ctl-Tlc-Tr equilibrium points as in orthopyroxene-rich settings. Further details on the consequences of variable compositions of the reacting rocks on the compositions of fluids generated during low temperature and high temperature alteration of ultramafic rocks can be found in Leong and Shock (2020) and Klein et al. (2013), respectively.

S2. Statistical Analyses

Statistical analyses were conducted to evaluate if compositional differences between different fluid types are significant. All calculations were performed using the Past *v4.03* statistical software (Hammer et al., 2001). Non-parametric Mann-Whitney U-tests were conducted to evaluate differences in the median values of dissolved species measured from hyperalkaline fluids (pH >11) collected at sites near or far from the basal thrust of the Samail ophiolite. The U-values, z-score, and *p*-values calculated using the Mann-Whitney U-test are compiled in Figure S2. Results of calculations show that the Cl, Na, and K concentrations of fluids collected from sites near and far from the basal thrust are significantly different at $p < 0.01$. Results from the Mann-Whitney U-test calculations, however, show that the DIC concentrations of fluids hosted near the basal thrust, which

are typically higher, are significantly different (at p <0.05) from those hosted far from the basal thrust.

Multivariate statistical analyses (analysis of similarities or ANOSIM, at 9,999 permutations) were conducted to evaluate if the O and H stable isotopic compositions of fluids sampled from different study sites are distinct from each other. Results of calculations are shown in Table S4, where study sites are arranged according to their locations. Most sites have isotopic compositions that are not significantly distinct, though the stable isotopic compositions of water at a given site can be significantly different from another site that is geographically further away. Samples collected from Shumayt and Al Bana have stable isotopic compositions that are the most distinct amongst the study sites.

Both Non-metric Multidimensional Scaling (NMDS) and ANOSIM were conducted to evaluate distinctions among various fluid types informed by simulations of subsurface reaction pathways and subsequent mixing processes. The pH and the square root of the molal concentrations of Mg, Si, Ca, DIC, Na, K, and Cl of investigated fluids identified as Type 1, intermediate, Type 2 and mixed in Figure 7 were used in the statistical analyses. Results of NMDS calculations are shown in a scatter plot in Figure S6 and p-values derived from ANOSIM calculations (at 9999 permutations) are summarized in Table S5. Both analyses use the Euclidian similarity matrix. Stress value from the NMDS is low at 0.0043.

S3. Differences in the compositions of ultramafic- and gabbro-hosted fluids

Most simulations of gabbro alteration are focused at high temperature and pressure conditions such as those occurring in submarine hydrothermal systems (McCollom and Shock, 1998; Palandri and Reed, 2004; Bach and Klein, 2009; Bach and others, 2013, Seyfried and others, 2015). Predictions of fluid compositions arising during interactions between meteoric water and gabbroic rocks in the continental subsurface are far scarcer. Gabbroic rocks comprise approximately a third of the surface exposures of the Samail ophiolite (Nicolas et al., 2000) and are also common in many other ophiolites. Gabbro-hosted hyperalkaline fluids are also documented in several studies (Neal and Stanger, 1985; Dewandel et al., 2005; Paukert et al., 2012; Chavagnac et al., 2013b; Cardace et al., 2013; Rempfert et al., 2017), and many of these springs occur near the gabbro-ultramafic contact. The influence of ultramafic rocks underlying the gabbroic rocks on the compositions of hyperalkaline fluids seeping out from gabbroic outcrops is largely unknown.

Reported compositions of gabbro-hosted fluids in the Samail ophiolite, together with those from this work, are plotted as orange symbols in Figure S7, where they can be compared with fluids documented in ultramafic environments (grey symbols). Compositions of most gabbro-hosted fluids overlap those hosted in ultramafic rocks. However, there are some notable differences that could be attributed to fluid-mineral reactions enabled when fluids encounter gabbroic rocks. Mineral solubility calculations were conducted to provide preliminary insights into how various minerals or mineral assemblages can account for these aqueous trends. Solubility calculations for 25°C and 1 bar were conducted using the same software package and thermodynamic data

described in the method section of this paper. Results of calculations are plotted as red curves in Figure S7.

Gabbro- and ultramafic-hosted Type 1 fluids (circumneutral, pH 7-9) have overlapping total dissolved Si values as shown in Fig S7a. In contrast, some of the highest dissolved Si values measured in Type 2 fluids (hyperalkaline, pH >11) are from gabbro-hosted fluids. This could be attributed to the higher silica content of gabbros, which can lead to the precipitation of secondary minerals with higher silica contents than serpentine and brucite such as talc, quartz, chlorite, zeolites and clay minerals. As shown in Figure S7a, all fluids hosted in either gabbroic or ultramafic rocks are below amorphous silica saturation. Type 1 fluids hosted in both lithologies are typically above quartz saturation while Type 2 fluids are usually well below saturation with respect to quartz and the chrysotile-talc equilibrium assemblage. Type 2 fluids hosted in ultramafic rocks approach equilibrium with serpentine and brucite. In contrast, despite overlapping with fluids hosted in ultramafic rocks as shown in Figure S7a, the Si concentrations of gabbro-hosted fluids do not approach the low values dictated by chrysotile-brucite equilibrium. This trend is likely to be attributed to the geological setting of gabbro-hosted hyperalkaline springs, many of which occur near the gabbro-ultramafic lithological contact. As gabbros are stratigraphically above peridotites in the Samail ophiolite, it is likely that deep-seated fluids would have first reacted with ultramafic rocks before encountering gabbroic rocks on their way to discharge at the surface. Such a scenario is analogous to ultramafic to gabbro mass transfer processes at high temperatures that have been proposed to facilitate the formation of rodingites (Bach and Klein, 2009; Bach et al., 2013).

As shown in Figure S7b, there are no noticeable differences in the Mg concentrations of Type 1 fluids hosted in either ultramafic or gabbroic rocks. As in the case of ultramafic-hosted fluids, Mg concentrations of Type 1 gabbro-hosted fluids rarely fall below values dictated by magnesite solubility. On the other hand, there are some noticeable differences between the Mg concentrations of Type 2 hyperalkaline fluids in these two lithological environments. Some of the most Mg-depleted Type 2 fluids were sampled from gabbroic-hosted springs. Unlike most ultramafic-hosted samples, some gabbro-hosted samples have Mg values below those set by brucite solubility. These lower Mg concentrations could be attributed to the precipitation of relatively Si-rich Mg-silicate minerals (e.g., talc, saponite, chlorite) that commonly occur in altered mafic rocks. As an example, as depicted in Figure S7b, lower Mg concentrations can be attained if fluids are in equilibrium with chrysotile and talc. As with Si, more constraints can be provided on the Mg concentrations of fluids dictated by the solubility of aluminum-bearing silicates such as chlorite, zeolite and clay minerals that are commonly observed in gabbroic rocks altered at low temperatures (Bach et al., 2001).

Dissolved Ca concentrations of Type 2 fluids from both gabbro and ultramafic bodies have similar trends that follow the solubility of calcite as shown in Figures 5c and S4c. However, total calcium concentrations in Type 1 fluids are somewhat more enriched in gabbro-hosted fluids than ultramafic-hosted fluids. Type 1 fluids, as discussed in the main text of this work, are products of early stages of reaction progress dictated by the dissolution of protolith minerals. Gabbroic rocks are more enriched in Ca compared to

ultramafic rocks due to the more abundant presence of Ca-plagioclase (anorthite) and Ca-clinopyroxene (diopside).

Like Ca, dissolved Na concentrations of Type 1 fluids hosted in gabbros are elevated compared to those hosted in ultramafic rocks as shown in Figure S7d. This could be attributed to the relatively elevated Na content of gabbroic rocks. However, similar observations can also be made for the dissolved Cl values of gabbro-hosted fluids plotted in Figure S7e, suggesting that leaching from salt minerals could be an alternative source for both Na and Cl. Figure S7f, however, shows no apparent differences between K trends of both gabbro- and ultramafic-hosted fluids, suggesting that leaching could be attributed only to halite (NaCl). In addition, leaching from other Na-bearing phases (*e.g.*, plagioclase and pyroxenes) can also occur concomitantly, as gabbro-hosted Type 1 fluids are typically more enriched in Na relative to Cl compared to Type 1 fluids hosted in ultramafic rocks as shown in Figure S7g.

As shown in Figure S7h, the total dissolved aluminum concentrations of Type 1 gabbro-hosted fluids overlap with those hosted in ultramafic rocks, but gabbro-hosted Type 2 fluids have elevated total dissolved Al values, closely following those dictated by the solubility of gibbsite, as shown in Figure S7h. In contrast, all ultramafic-hosted Type 2 fluids remain highly undersaturated with respect to gibbsite, which is not surprising as ultramafic rocks are typically depleted in Al. Chavagnac and others (2013b) documented Al-bearing layered double hydroxides such as hydrotalcite and indigirite in gabbro-hosted hyperalkaline pools marked by elevated dissolved Al content.

Further insight into the underlying mineral controls on the compositions of gabbro-hosted fluids, in comparison to those hosted in ultramafic rocks, can be revealed through mineral activity diagrams. Activities of several aqueous species ($SiO_{2(aq)}$, Ca^{+2}, H^{+}) were evaluated from the measured values using the same thermodynamic database as all other calculations in this study and are plotted in an activity diagram for the CaO-Al_2O_3-SiO_2-H_2O (phase boundaries as orange lines, balanced on Al_2O_3) and CaO-MgO-SiO_2-H_2O system (black lines, balanced on MgO) systems shown in Figure S8. Calculated activities ($a Ca^{+2}/(a H^{+})^2$, $a SiO_2$) of gabbro- (orange symbols) and ultramafic-hosted (grey symbols, values similar to Figure 5f) fluids are overlain in the activity diagram. Gabbro-hosted hyperalkaline fluids typically have similar calcium to hydrogen activity ratios ($a Ca^{+2}/(a H^{+})^2$) as those hosted in ultramafic bodies but are characterized by having somewhat higher silica activities ($a SiO_2$). As shown in Figure S8, these gabbro-hosted fluids seem to be drawn to equilibrium with gibbsite, grossular (garnet), and prehnite, unlike ultramafic-hosted fluids that approach equilibrium with chrysotile and brucite resulting in lower $a SiO_2$. Similarly, Type 1 fluids hosted in gabbroic rocks mostly have overlapping $a Ca^{+2}/(a H^{+})^2$ with those hosted in ultramafic rocks but tend to have higher $a SiO_2$. These gabbro-hosted fluids are within the stability field of scolecite and beidellite, which are minerals that belong to the zeolite and smectite groups, respectively. In addition to ultramafic rocks, the Oman Drilling Project (Kelemen et al., 2013) has recovered gabbroic rocks. Examination of low-temperature secondary phases from recovered cores would provide constraints on which minerals dictate the evolution of fluids during fluid-gabbro interactions. Thermodynamic simulations of low-temperature fluid-gabbro interactions and eventually testing these models with more comprehensive

and in-depth investigations of gabbro-hosted fluids will bridge our current knowledge gap in this poorly explored fluid-rock system. Gabbros are the most common rocks that comprise the oceanic crust and are also common in ophiolites. Results of this future work can potentially inform future biogeochemical studies on the likelihood of these vast lithological systems to host habitable environments.

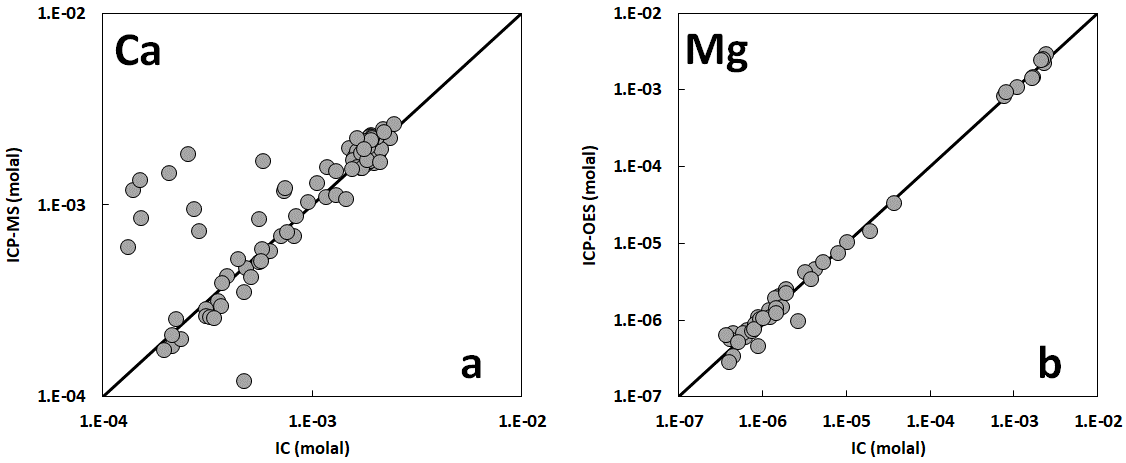

Figure S1. Comparison of analytical results of dissolved Ca (a) and Mg (b) determined through the ICP-MS and ICP-OES, respectively, versus that determined through the IC.

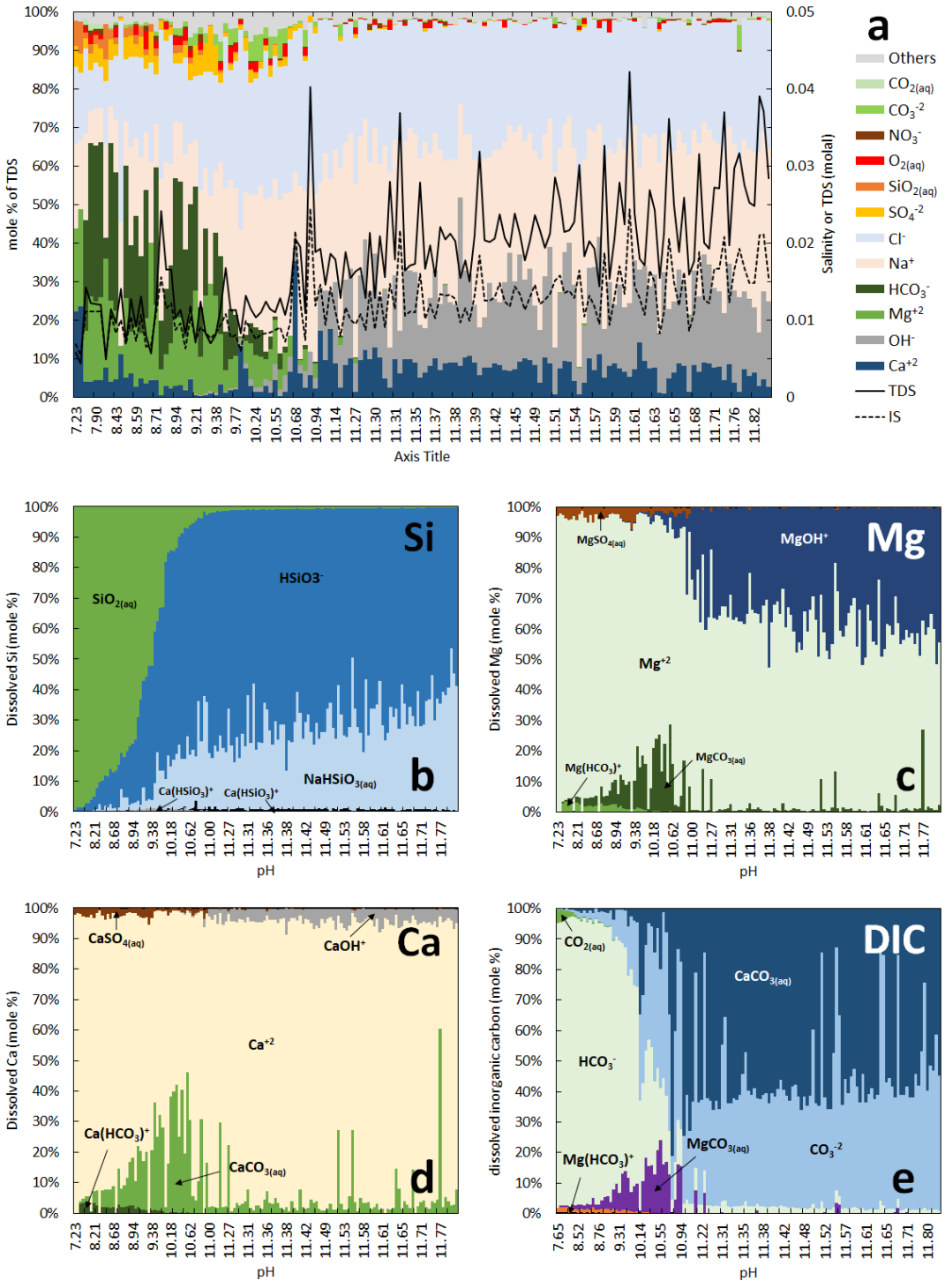

Figure S2. (a) Total dissolved solutes (TDS, solid black line) and ionic strength (IS, dashed black line) of sampled fluids (values at right of plot), arranged with increasing pH from left to right. Component species of the total dissolved solutes (in mole %) are represented by the colored field. Also shown are component species that comprise the total dissolved Si (b), Mg (c), Ca (d), and inorganic carbon (e).

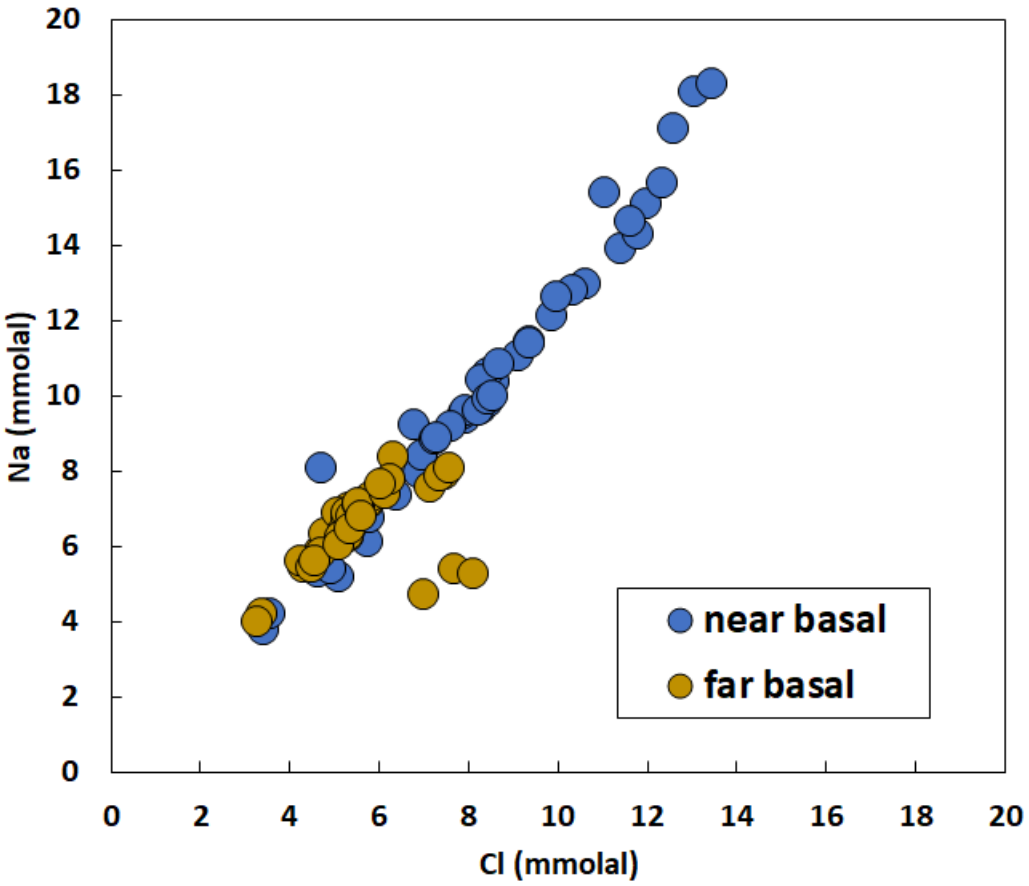

Figure S3. Dissolved Na and Cl concentrations of hyperalkaline fluids (pH >11) sampled at study sites close to the basalt thrust (blue circles) and those sampled far within the ophiolite (brown circles, mostly near the peridotite-gabbro contact).

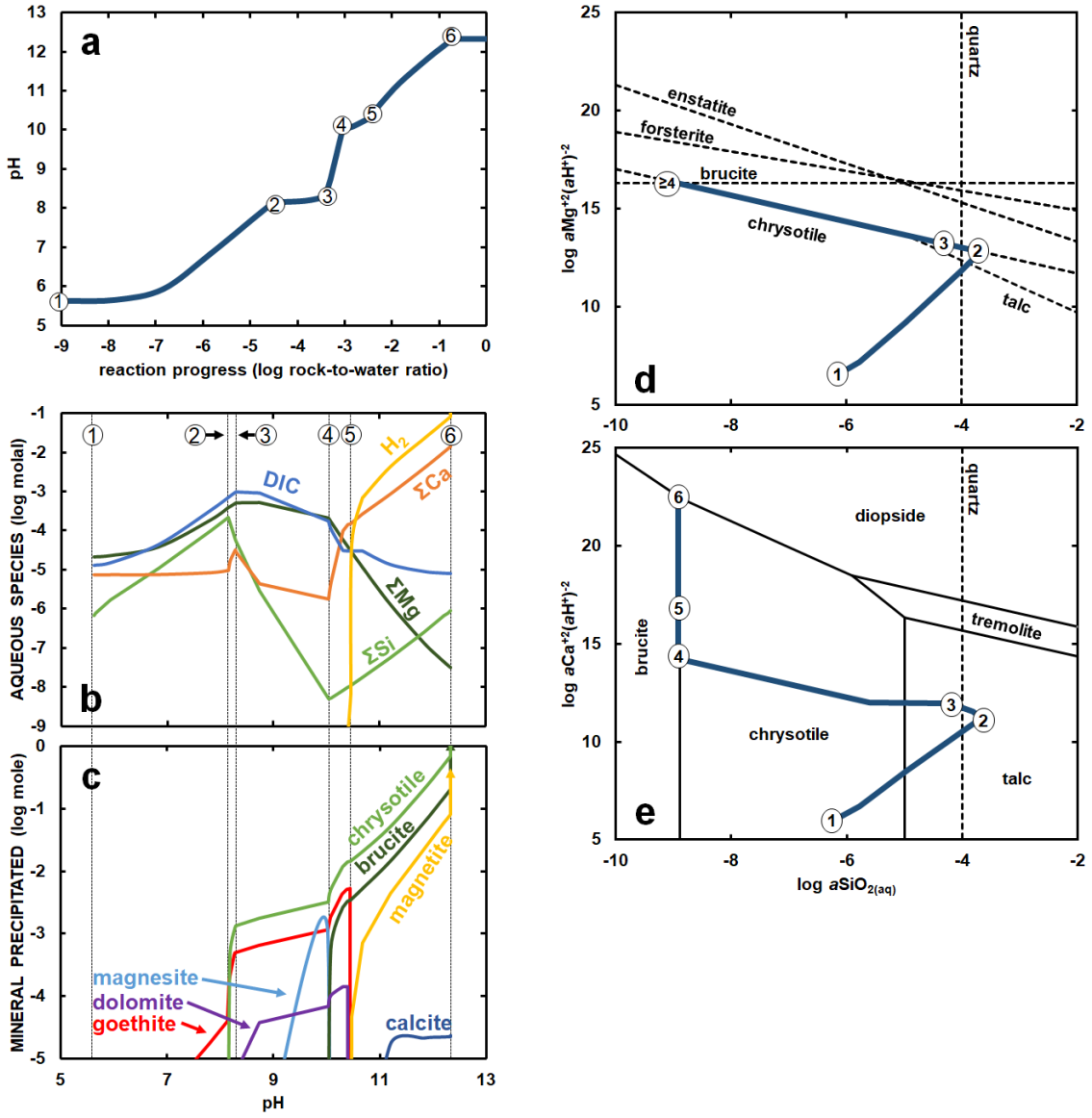

Figure S4. Reaction paths simulating serpentinization of an ultramafic rock with the composition 85% olivine-14% orthopyroxene-1% clinopyroxene. (a) depicts the increase in pH as serpentinization progresses, highlighting six stages discussed in the text. Progress of the serpentinization process is depicted in rock-to-water ratio (*e.g.*, log value of -3 represents reaction of 1 g of reacted ultramafic rock in 1000 g water). (b) and (c) depict changes in the concentrations of aqueous species (in log molality) and amount of minerals precipitated (in log moles) with pH, respectively. Reaction paths are plotted on activity diagrams for the (d) MgO-SiO_2-H_2O and (e) CaO-MgO-SiO_2-H_2O systems. Dashed lines in (d) and (e) indicate saturation of indicated minerals, while solid lines in (e) represent boundaries for the stability fields of minerals. Dark blue curves show results of reaction path calculations. Numbers indicate the starting points of the six stages of serpentinization.

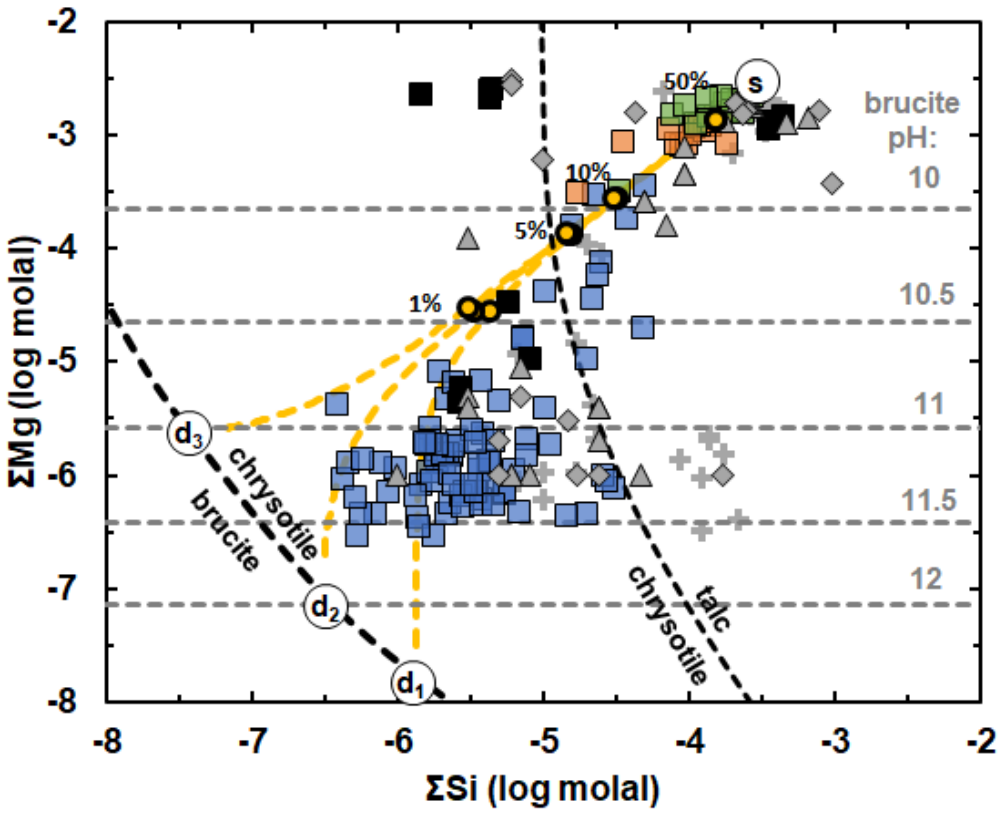

Figure S5. Plot showing the Mg versus Si concentrations of sampled fluids, as well as the mixing path described in Figure 5. Symbols shown are similar to that depicted in Figures 3, 5, 8, and 9. In addition, the horizontal gray dashed lines depict saturation line for brucite, given the pH indicated above these lines. Note that in cases where the Si concentrations of fluids exceed that depicted by the brucite-chrysotile equilibrium line (lower left dashed black curve), brucite is metastable with respect to chrysotile, talc and quartz (not shown). At pH = 9, quartz can be saturated when Si concentration is 10^{-4} molal while at higher pH, quartz can be saturated at higher Si concentrations. Note that while Mg concentrations of samples tend to plot from the mixing line towards the brucite saturation line at variable pH, the Si concentrations that are far lower than that depicted in the mixing curve are rare. A few samples with low Si ($<10^{-5}$ molal) and high Mg ($>10^{-3}$ molal) concentrations can be accounted for by intermediate stages of the subsurface serpentinization pathway (see dark blue curve in Figure 5a).

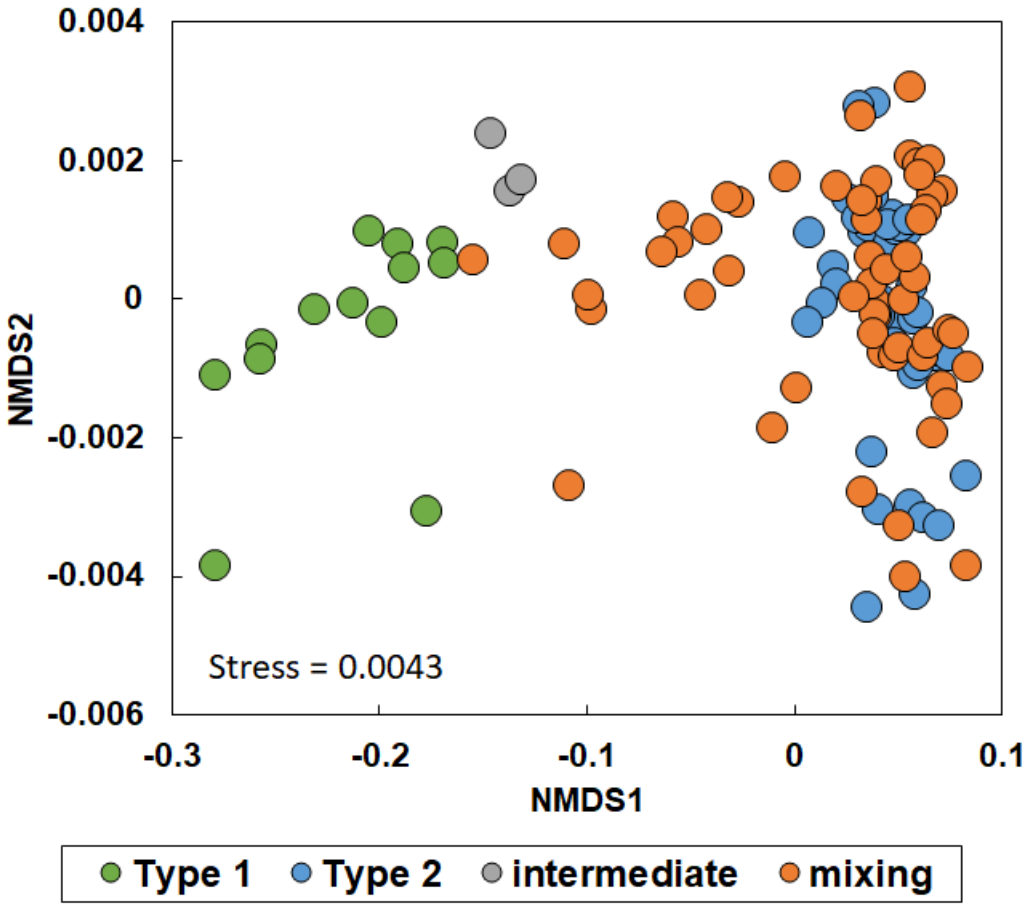

Figure S6. Results of Non-metric Multidimensional Scaling (NMDS) ordination depicted in a scatter biplot. A circle depicts an individual sample, and its color represents its classification as shown in Figure 7. Samples that are more similar to one another are ordinated closer together. The axes as well as the orientation of the plot are arbitrary. Stress value is low at 0.0043.

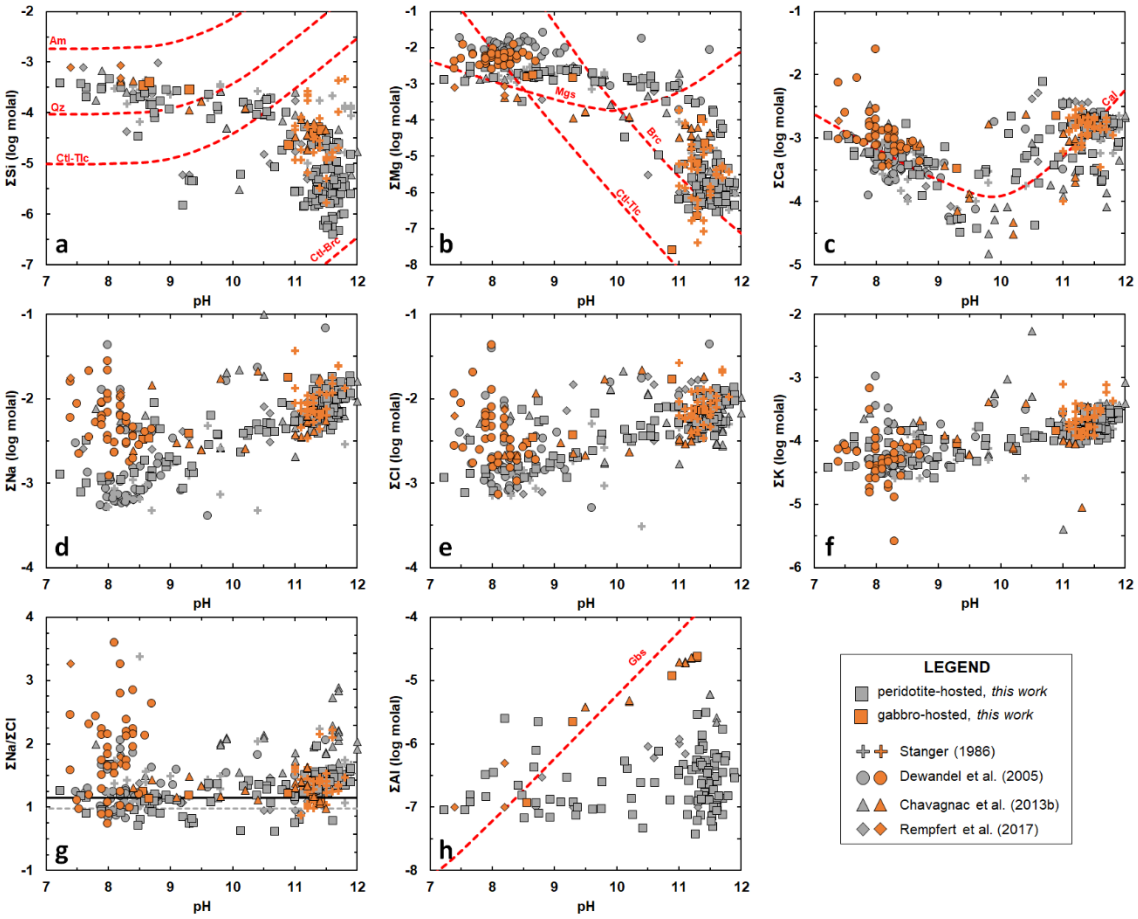

Figure S7. Comparison between ultramafic-hosted (grey symbols) and gabbroic-hosted (orange symbols) fluids in Oman. Symbol shapes and data sources are the same as in Figure 3. Trends in the total dissolved Si (a), Mg (b), Ca (c), Na (d), Cl (e), K (f), ratio between total dissolved Na and Cl (g), and total dissolved Al (h) with pH are shown. Dashed red lines and curves show solubility conditions for various minerals: Am – amorphous silica, Qz – quartz, Ctl – chrysotile, Tlc – talc, Brc – brucite, Mgs – magnesite, Cal – calcite, Gbs – gibbsite.

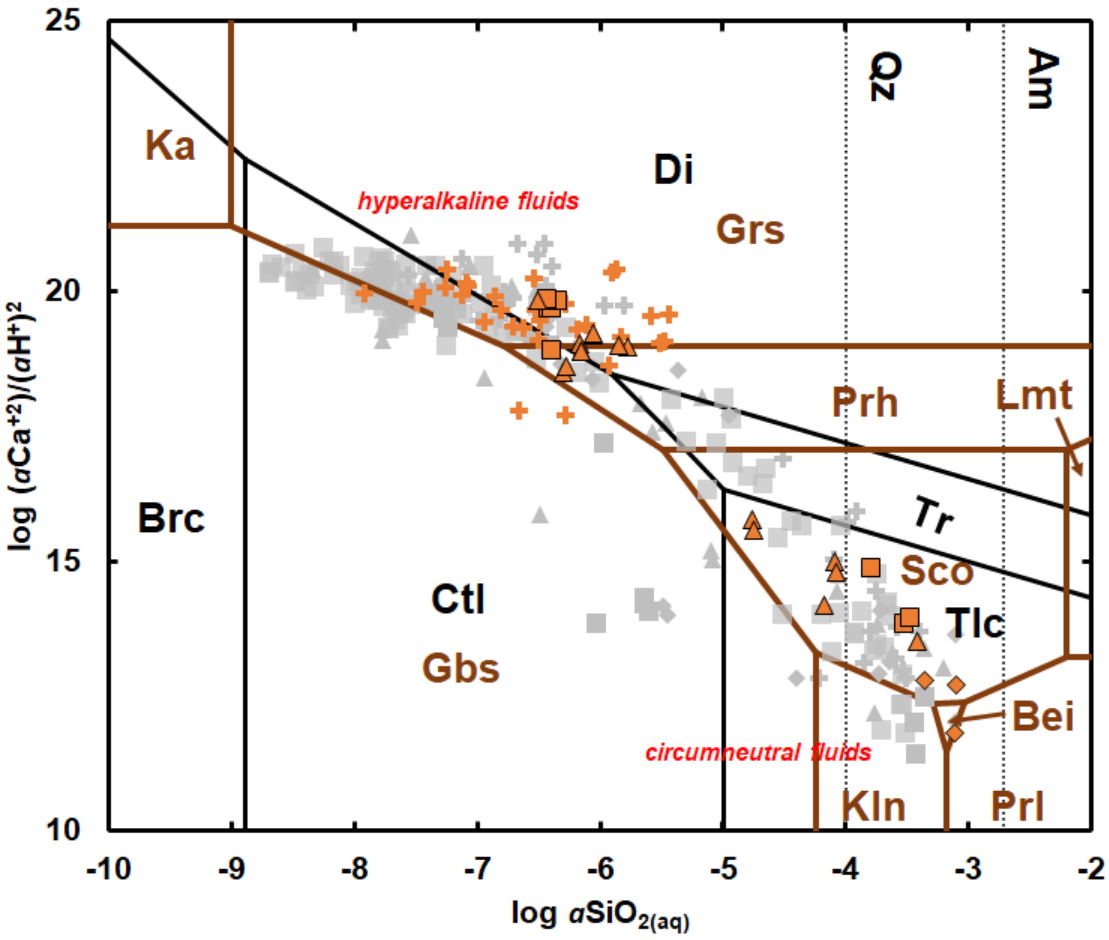

Figure S8. Log $a\mathrm{Ca}^{+2}/(a\mathrm{H}^{+})^{2}$ *vs* $a\mathrm{SiO}_2$ of gabbro-hosted fluids (various symbols in orange) plotted on an activity diagram for the CaO-Al_2O_3-SiO_2-H_2O system (phase boundaries as orange lines) at 25°C, 1 bar. Underlying it is an activity diagram for the CaO-MgO-SiO_2-H_2O system (black lines) and plotted activities of ultramafic-hosted fluids (various symbols in grey), similar to those shown in Figure 5f. Symbols are the same as in Figure S1. Note that the lines represent stability boundaries between the indicated minerals: Brc – brucite; Ctl – chrysotile; Tlc – talc; Tr – tremolite; Di – diopside; Qz – quartz; Am – amorphous SiO_2, Gbs – gibbsite; Kln – kaolinite; Prl – pyrophyllite; Bei – beidellite; Sco – scolecite: Lmt – laumontite; Prh – prehnite; Grs – grossular; Ka – katoite. Thermodynamic properties of minerals are taken from Helgeson et al. (1978) and Wolery and Jove-Colon (2004).

Table S1. Field and laboratory measurements for samples collected in this study.

Table S2. Saturation states of various relevant minerals.

	Mann-Whitney U-test		
Species	**U value**	**z-score**	**p-value**
Cl	294	5.5143	<0.0001
Na	292	5.5313	<0.0001
K	248	5.9055	<0.0001
Si	824	1.0076	0.31363
Mg	713	1.9516	0.05099
Ca	836	0.90564	0.36513
DIC	641	2.2533	0.02424
pH	727	1.8325	0.06687

Table S3. Results of Mann-Whitney U-test of hyperalkaline fluids (pH >11) sampled closed to or far from the ophiolite's basalt thrust.

Sites	NSHQ14	Dima	Qafifah	Falaij	Al Hilayw	Misbit	SJA	WDA	Al Bana	Shumayt	Sudari
NSHQ14		1	1	1	1	1	1	1	1	0.0495	1
Dima	1		1	1	1	1	1	1	1	0.011	1
Qafifah	1	1		1	0.4675	0.033	0.1925	1	0.0055	0.0055	0.275
Falaij	1	1	1		0.4345	0.0055	0.022	1	0.0055	0.0055	0.0165
Al Hilayw	1	1	0.4675	0.4345		1	1	1	0.0165	0.011	1
Misbit	1	1	0.033	0.0055	1		1	1	0.055	0.022	1
SJA	1	1	0.1925	0.022	1	1		1	0.198	0.11	1
WDA	1	1	1	1	1	1	1		1	0.011	1
Al Bana	1	1	0.0055	0.0055	0.0165	0.055	0.198	1		0.0055	0.7975
Shumayt	0.0495	0.011	0.0055	0.0055	0.011	0.022	0.11	0.011	0.0055		0.033
Sudari	1	1	0.275	0.0165	1	1	1	1	0.7975	0.033	

Note 1: Sites are arranged in this table according to their location, with those sampled from the southeastern part of the ophiolite (starting with NSHQ14) at the top/left to those sampled in the northern part of the ophiolite at the bottom/left.

Note 2: p-values in blue indicate sites where isotopic compositions are significantly different at p <0.05.

Table S4. *p*-values derived from ANOSIM calculations of the water isotopic compositions of fluids collected from various sites.

Fluid Type	circumneutral	intermediate	mixed	hyperalkaline
circumneutral		0.0618	0.0006	0.0006
intermediate	0.0618		0.0006	0.0024
mixed	0.0006	0.0006		1
hyperalkaline	0.0006	0.0024	1	

Note: *p*-values indicating statistical significance at $p < 0.05$ are marked as blue.

Table S5. Bonferroni-corrected p-values derived from ANOSIM between different fluid types.

	Surface Fluid (s)[1]	Deep Subsurface Fluid 1 (d_1)[2]	Deep Subsurface Fluid 2 (d_2)[3]	Deep Subsurface Fluid 3 (d_3)[4]
pH	7.9	12.3	11.7	11.1
Na (mmolal)[5]	1.14	10	10	10
Ca (mmolal)	0.56	14.4	3.2	0.7
Mg (µmolal)	2810	0.03	0.2	2.6
Cl (mmolal)[5]	1.28	10	10	10
Si (µmolal)	303	1.3	0.3	0.1
DIC (µmolal)	5120	8	10	20

[1]composition taken from sample 140116B. Sample is closest to predicted compositions in equilibrium with secondary phases common in the shallow subsurface.

[2]fluid in equilibrium with the Ctl-Brc-Di and calcite assemblage at 25°C and 1 bar.

[3]fluid in equilibrium with the Ctl-Brc-Cal assemblage, given 10 µmolal DIC, at 25°C and 1 bar.

[4]fluid in equilibrium with the Ctl-Brc-Cal assemblage, given 20 µmolal DIC, at 25°C and 1 bar.

[5]Deep fluids were given Na and Cl concentrations of 10 mmolal as an average of the range of concentrations (3-20 mmolal) observed in environmental samples

Table S6. Composition of fluids used in mixing calculations.